



Published in final edited form as:

Nat Neurosci. 2014 May ; 17(5): 694–703. doi:10.1038/nn.3691.

## Astrocyte Kir4.1 ion channel deficits contribute to neuronal dysfunction in Huntington's disease model mice

Xiaoping Tong<sup>\*,1</sup>, Yan Ao<sup>\*,2</sup>, Guido C. Faas<sup>3</sup>, Sinifunanya E. Nwaobi<sup>4</sup>, Ji Xu<sup>1</sup>, Martin D. Haustein<sup>1</sup>, Mark A. Anderson<sup>2</sup>, Istvan Mody<sup>1,3</sup>, Michelle L. Olsen<sup>4</sup>, Michael V. Sofroniew<sup>2,Ψ</sup>, and Baljit S. Khakh<sup>1,2,Ψ</sup>

<sup>1</sup>Department of Physiology, David Geffen School of Medicine, University of California Los Angeles, Los Angeles USA CA 90095–1751

<sup>2</sup>Department of Neurobiology, David Geffen School of Medicine, University of California Los Angeles, Los Angeles USA CA 90095–1751

<sup>3</sup>Department of Neurology, David Geffen School of Medicine, University of California Los Angeles, Los Angeles USA CA 90095–1751

<sup>4</sup>Department of Cell, Developmental and Integrative Biology, University of Alabama at Birmingham, Birmingham, AL 35294

### Abstract

Huntington's disease (HD) is characterized by striatal medium spiny neuron (MSN) dysfunction, but the underlying mechanisms remain unclear. We explored roles for astrocytes, which display mutant huntingtin in HD patients and mouse models. We found that symptom onset in R6/2 and Q175 HD mouse models is not associated with classical astrogliosis, but is associated with decreased Kir4.1 K<sup>+</sup> channel functional expression, leading to elevated *in vivo* levels of striatal extracellular K<sup>+</sup>, which increased MSN excitability *in vitro*. Viral delivery of Kir4.1 channels to striatal astrocytes restored Kir4.1 function, normalized extracellular K<sup>+</sup>, recovered aspects of MSN dysfunction, prolonged survival and attenuated some motor phenotypes in R6/2 mice. These findings indicate that components of altered MSN excitability in HD may be caused by heretofore unknown disturbances of astrocyte-mediated K<sup>+</sup> homeostasis, revealing astrocytes and Kir4.1 channels as novel therapeutic targets.

Users may view, print, copy, and download text and data-mine the content in such documents, for the purposes of academic research, subject always to the full Conditions of use:[http://www.nature.com/authors/editorial\\_policies/license.html#terms](http://www.nature.com/authors/editorial_policies/license.html#terms)

Editorial/manuscript correspondence to BSK: Department of Physiology, David Geffen School of Medicine, University of California, Los Angeles, 10833 Le Conte Avenue, 53–263 CHS, Los Angeles, CA 90095–1751, Fax: 310 206 5661, Tel : 310 825 6258, [bkhakh@mednet.ucla.edu](mailto:bkhakh@mednet.ucla.edu).

\*authors with equal contributions to experiments (XT and YA)

ΨThese authors jointly directed the work: BSK (electrophysiology and cloning), [bkhakh@mednet.ucla.edu](mailto:bkhakh@mednet.ucla.edu) and MVS (immunohistochemistry and behavior), [Sofroniew@mednet.ucla.edu](mailto:Sofroniew@mednet.ucla.edu)

**Author contributions:** XT, JX, MDH, and BSK did the molecular biology, imaging and electrophysiology experiments. YA, MAA and MVS did the immunohistochemistry, Westerns and behavior experiments. GCF and IM did the potassium concentration measurements. SEN and MLO did the qPCR experiments. BSK and MVS directed the work. BSK wrote the first draft of the paper. All authors contributed to the final version of the manuscript.

Supplementary information included as a separate file: 15 figures, 4 tables and detailed methods

Astrocytes contribute to the function of neurons and the brain<sup>1-3</sup>. There is also growing appreciation that astrocytes contribute to neurological and psychiatric diseases<sup>2,4-6</sup>. HD is an autosomal dominant disorder characterized by progressive motor, cognitive and psychiatric disturbances associated with neuronal dysfunction and atrophy of the striatum and other brain regions. HD is caused by an expanded chain of polyglutamines localized to the N-terminal region of the huntingtin protein (HTT) that causes intracellular accumulation and aggregation of mutant huntingtin<sup>7</sup>. The physiological role of HTT and the mechanisms that produce the disease are largely unknown, although intense effort has focused on the study of mutant huntingtin (mHTT) expression on neuronal function, particularly in the striatum<sup>8</sup>. Recent studies suggest that astrocytes may also be involved in HD. Thus, brains from HD patients and from mouse models of HD show accumulation of mHTT in striatal astrocytes<sup>9,10</sup>. Selective expression of mHTT only in astrocytes leads to cell death of striatal neurons<sup>9</sup>, reduced glutamate transporter expression<sup>10</sup> and age-dependent broadly HD-like pathology<sup>11</sup>. However, these studies do not prove that astrocyte physiology is altered in conventional mouse models of HD.

An appraisal of existing animal models of HD does not reveal that any one is superior<sup>12</sup>, and so we explored astrocyte physiology in two mouse models of HD: an early onset well established “aggressive” exon 1 human mHTT transgenic R6/2 model<sup>7</sup> and the more slowly developing knock-in Q175 model<sup>13,14</sup>. We found that Kir4.1 potassium ion channel expression was significantly decreased in astrocytes that express mHTT, with little or no evidence for reactive astrogliosis at stages corresponding with initial onset of symptoms in both mouse models. The loss of a resting K<sup>+</sup> conductance depolarized astrocytes and likely contributed to the elevated levels of K<sup>+</sup> that we measured *in vivo* within the striatum of HD model mice. Moreover, we found that these subtly elevated extracellular K<sup>+</sup> levels (by ~2 mM) significantly depolarized medium spiny neurons (MSN) and increased their excitability. Conversely, rescuing the loss of astrocyte Kir4.1 channels ameliorated several deficits associated with HD mouse models. We propose the novel hypothesis that some features of MSN dysfunction in HD are secondary to disturbances of astrocyte Kir4.1. These data thus reveal astrocytes as potential cellular targets for therapeutic development in HD.

## Results

We performed evaluations for R6/2 and Q175 mouse models of HD<sup>7,13,14</sup>. To avoid repetition, the text mainly reports data from WT and R6/2 mice at presymptomatic (P30) and symptomatic ages (P60–80; Supp Fig. 1a-d). However, key experiments were repeated with WT, heterozygous and homozygous Q175 mice at ages of 2–3 months, 6–7 months and 9–12 months. These data are reported throughout the results and the Supplementary information.

### No striatal astrogliosis in R6/2 mice at symptomatic ages

Reactive astrogliosis is associated with injury, neuroinflammation and disease and is classically regarded as being accompanied by easily detectable increases in astrocyte GFAP expression and morphological changes<sup>15</sup>. Using immunohistochemistry we detected only low levels of striatal GFAP immunostaining that was indistinguishable in R6/2 and WT

mice at P60–80 (Fig. 1a; n = 4 mice), implying little or no astrogliosis. Quantification of individual GFAP expressing astrocytes from WT and R6/2 mice at P70 provided no evidence of cellular hypertrophy or any detectable morphological changes associated with classical astrogliosis<sup>15</sup> (Fig. 1b–e; n = 4 mice; 32 astrocytes). Using Ki67 immunostaining we also found no evidence of astrocyte proliferation in R6/2 mice at P60–80, or even at P110, a time of considerable tissue loss (Supp Fig. 2; n = 5). pSTAT is a transcriptional regulator that is strongly increased during classical astrogliosis<sup>19</sup>, but we found no evidence for upregulation of pSTAT3 in R6/2 mice at P60–80 (data not shown; n = 4). Lastly, using Western blot analysis of CP tissue, we found no evidence for increased GFAP expression in R6/2 mice at P60–80 relative to WT littermates (Fig. 1f; n = 4). In contrast, in older R6/2 mice (P104–110), when overt striatal atrophy and neurodegeneration has occurred, there was clear evidence of astrogliosis in the form of GFAP upregulation (Supp Fig. 3).

Our analysis of astrogliosis is consistent with early observations on GFAP expression in R6/2 mice<sup>7</sup> and suggests that HD-like symptoms in the mice occur before overt astrogliosis. In humans, a doubling of GFAP expression is observed in late stages of HD (Grades 3 and 4), but at Grade 0 no statistically significant differences from control are reported<sup>10</sup>.

### Striatal astrocytes display altered properties in HD mice

In contrast to GFAP, which marked only a small number of striatal astrocytes (Fig. 1a; n = 6), Aldh1L1<sup>16</sup>, GS and S100 $\beta$  marked most striatal astrocytes (Supp Fig. 4). Co-localization experiments showed that all GS expressing astrocytes were Aldh1L1 positive, and all Aldh1L1 expressing astrocytes were also S100 $\beta$  positive (Supp Fig. 5; n = 4). Next, we used triple color IHC to determine if GFAP, Aldh1L1, GS and S100 $\beta$ -expressing astrocytes (in green) contained mHTT nuclear inclusions (nuclei in blue, inclusions shown in white; Fig. 2a) using the monoclonal mEM48 antibody that recognizes exon 1 of mHTT<sup>17</sup>. We found that the nuclei of GFAP, S100 $\beta$ , GS and Aldh1L1-labelled astrocytes were positive for mHTT (Fig. 2a; n = 4), reminiscent of past work<sup>9,10</sup>.

Using morphological and electrophysiological criteria<sup>18</sup> to identify astrocytes in brain slices (Supp Fig. 6), we found that R6/2 astrocytes were significantly more depolarized than WT astrocytes at P60–80 (resting membrane potentials were  $-76 \pm 0.7$  and  $-71 \pm 0.8$  mV for WT and R6/2 astrocytes, respectively; n = 79 & 67,  $P < 0.0001$  using a two tailed Mann–Whitney test). These differences were not observed at P30 (Fig. 2b,c; Supp Table 1; n = 53–55,  $P = 0.794$  using a two tailed Mann–Whitney test). At these same ages, striatal R6/2 astrocytes displayed significantly lower membrane conductances (Fig. 2d) and showed higher membrane resistances (Fig. 3a–d; Supp Table 1; n = 53–79,  $P < 0.0001$  using a two tailed Mann–Whitney test). There were no significant differences in membrane capacitance at P30 or P60–80 (capacitance was 18–19 pF in each case, data not shown; n = 53–79 cells).

Differences in striatal astrocytes between WT and R6/2 mice at P60–80 did not extend to hippocampal astrocytes from R6/2 and WT mice at P30 and P60–80 (Supp Table 1; n = 7–11). To ascertain whether the differences between WT and R6/2 striatal astrocytes were restricted to the R6/2 mouse model, we repeated all the electrophysiology experiments in WT, heterozygous and homozygous Q175 mice at 2–3, 6–7 and 9–12 months of age (Supp Tables 2–3; n = 11–34). These data show that astrocytes from Q175 homozygous and

heterozygous mice are also significantly more depolarized and display lower membrane conductances at ages when HD-like symptoms are manifest, i.e. 6–7 months for homozygous mice and 9–12 months for heterozygous mice (Supp Tables 2–3;  $n = 11–34$ ).

### Striatal astrocytes from HD mice display reduced Kir4.1 currents

Weakly inwardly rectifying Kir4.1 channels are the predominant  $K^+$  channels in astrocytes<sup>19–21</sup> and underlie their negative resting membrane potentials near the potassium equilibrium potential<sup>22</sup> ( $E_K$ ). We explored the possibility that astrocytes from HD mouse models may display reduced Kir4.1 currents. To this end, we measured I/V relations before and during extracellular applications of the Kir4.1 channel blocker  $Ba^{2+}$  (100  $\mu$ M), and by subtracting the I/V traces (Supp Fig. 7) we isolated  $Ba^{2+}$ -sensitive Kir4.1 currents, which displayed reversal potentials ( $E_{rev}$ ) close to  $E_K$  (Fig. 3e,f; Supp Fig. 7)<sup>23</sup>. We repeated these experiments for WT and R6/2 mice at P30 and P60–80, as well as for WT, heterozygous and homozygous Q175 mice at 2–3, 6–7 and 9–12 months of age (Fig. 3e,f;  $n = 12–24$ ; Supp Tables 1–3). We found significant (up to 30%) reductions in  $Ba^{2+}$ -sensitive currents in astrocytes from HD-model mice (both R6/2 and Q175) at symptomatic ages, but not at ages that were pre symptomatic (Fig. 3e,f;  $n = 12–24$ ; Supp Tables 1–3). We also used nortriptyline (NOR; 300  $\mu$ M) which preferentially blocks Kir4.1 channels over other inward rectifiers<sup>24,25</sup>. The use of NOR showed that Kir4.1 currents were significantly reduced in R6/2 mice relative to WT at P60–80 (Supp Table 4;  $n = 13,14$ ).

We detected significant astrocyte electrophysiological changes in the 9–12 month age group for heterozygous Q175 mice. How does this relate to symptoms in these mice? Past work shows that heterozygous Q175 mice display significant behavioral changes at less than 6 months of age<sup>14</sup>. However, in other tests they display no phenotypic changes even when they are 12 months old, and they don't show decreased body weight until they are  $\sim 1$  year old<sup>14</sup> (but see ref<sup>13</sup>). Moreover, at a cellular level MSN properties are altered at different ages. Thus, these mice display a phenotypic spectrum that occurs at different ages<sup>14</sup>. We also make no claim that the astrocyte dysfunction we report is the only driver of behavioral/systemic disorder in HD mouse models.

### Mechanistic insights on reduced Kir4.1 currents in R6/2 mice

We used quantitative PCR (*qPCR*) to determine if Kir4.1 mRNA levels were decreased in R6/2 striatal tissue relative to WT (the gene name for Kir4.1 is *KCNJ10*). Although there was a trend for Kir4.1 mRNA levels to be  $\sim 10\%$  lower, this did not reach statistical significance (Fig. 4a;  $n = 7, 5$ ;  $P = 0.1688$  unpaired Student's *t* test). Consistent with our Western blot data (Fig. 1g), we found that GFAP mRNA levels were also not significantly changed in R6/2 mice relative to WT (Fig. 4b;  $n = 7, 5$ ;  $P = 0.0845$  unpaired Student's *t* test), and consistent with past studies<sup>26</sup> we found that Glt1-1 mRNA levels were significantly reduced in R6/2 mice (Fig. 4c;  $P = 0.0267$  unpaired Student's *t* test). For the aforementioned experiments, Kir4.1 mRNA levels were analyzed in relation to GAPDH, ATP5B and UBC as controls (Supp Fig 8a), because these mRNAs are among the most stable in mouse models of HD<sup>27</sup>. Thus Kir4.1 mRNA levels are not significantly reduced in R6/2 mice at symptomatic ages (P60–80), a finding that was reproduced with the WT, heterozygous and homozygous Q175 mice aged 10 months (Supp Fig. 8b;  $n = 4–5$ ). This recalls transcriptome

analysis of R6/2 mice at ~P63, but differs from human postmortem analysis, where Kir4.1 mRNAs were significantly, albeit subtly, reduced in Grade 3 stages of HD<sup>28</sup>.

mHTT can affect the function of some intracellular ion channels<sup>29</sup>, prompting us to explore whether mHTT directly affects the function of Kir4.1 channels. In order to test for this, we determined if mHTT with 145 polyglutamines (mHTT-Q145) affected Kir4.1-GFP channel function in HEK-293 cells. We measured equally sized total and Ba<sup>2+</sup>-sensitive Kir4.1 currents in HEK-293 cells expressing Kir4.1-GFP alone or Kir4.1-GFP and mHTT-Q145 (Fig. 4d-e; n = 15-17). Controls showed that mHTT-Q145 proteins were expressed in HEK-293 cells, implying that mHTT-Q145 does not directly affect Kir4.1 ion channel function.

We used Western blot analysis to determine if Kir4.1 protein levels were reduced in striatal tissue (relative to  $\beta$ -actin); we used Glt-1 as a positive control<sup>11</sup> (Fig. 4c). Western blot analysis showed significantly reduced levels of Kir4.1 proteins in striatal tissue from R6/2 mice at P60-80, but not at P30 (Fig. 4g; n = 4). Additionally, Glt-1 protein levels were reduced as expected (Fig. 4h; n = 4). Similar data were gathered for Q175 mice (Supp Fig. 9). We also found that glutamine synthetase (GS) levels were significantly reduced in R6/2 mice at P60-80 (Fig. 4g; n = 4), but only modestly in relation to the reductions that accompany astrogliosis<sup>15</sup>. Together, the electrophysiology and Western blot data provide compelling evidence (Figs. 3-4) for astrocyte Kir4.1 channel dysfunction in HD mouse models.

### mHTT expressing astrocytes display reduced Kir4.1 immunostaining

Using four color IHC (Fig. 5a,b), we studied astrocyte Kir4.1 expression in single cells immunostaining (red) in relation to nuclei (blue), mHTT nuclear inclusions (white) and S100 $\beta$  (green) for WT and R6/2 mice at P60-80 (Figs. 3 & 4). In these experiments, mHTT nuclear inclusions indicate which cells exhibit nuclear mHTT aggregates, but they do not tell us about the larger population of cells that may express soluble mHTT<sup>30</sup>. In WT mice, we observed no nuclear mHTT inclusions and robust expression of Kir4.1 in all S100 $\beta$  positive astrocytes (arrows 1-3 in Fig. 5a,c; n = 6 mice). In contrast, in R6/2 mice we observed strong nuclear mHTT staining in ~10% of S100 $\beta$  positive astrocytes at P30, with a significant increase to ~20% at P60-80 (Fig. 5b,c). We quantified Kir4.1 immunostaining in S100 $\beta$  positive astrocytes and found that astrocytes that were S100 $\beta$  positive and also contained mHTT displayed significantly lower levels of Kir4.1 immunostaining as compared with astrocytes in WT mice or astrocytes that did not contain mHTT inclusions in R6/2 mice (Fig. 5d). Together, these data show that a significant fraction of R6/2 S100 $\beta$  positive astrocytes (~20%) contain mHTT nuclear inclusions at the age of P60-80, and that these astrocytes display significantly reduced Kir4.1 immunostaining (Fig. 5d).

Why is it that ~20% of S100 $\beta$  positive astrocytes contain mHTT nuclear inclusions (Fig 5c), whereas we detected significantly decreased astrocyte Kir4.1 currents across a sampling of all recorded astrocytes? First, astrocytes are coupled by gap junctions<sup>31</sup>, thus single-cell recordings sample a population of astrocytes. Second, mHTT can exist in a soluble form and also within inclusions. Third, despite intense study it remains unclear if the major pathological form is the cytosolic or the nuclear inclusion version of mHTT<sup>30</sup>. In order to try

and explore the cytosolic form of mHTT we also tested the MW8 antibody, but found that this preferentially labeled inclusions (Supp Fig 10). We suggest that many astrocytes may contain soluble forms of mHTT not detected by mEM48 and that these lead to Kir4.1 dysfunction in populations of astrocytes; a subpopulation of these (~20%) contain mHTT nuclear inclusions detectable with mEM48.

### Astrocyte deficits are rescued by viral delivery of Kir4.1–GFP

The data reported in the preceding sections strongly suggest that Kir4.1 channel function and expression are compromised in striatal astrocytes from symptomatic HD mouse models. In light of this, we determined if viral delivery of Kir4.1 would rescue the deficits observed in HD mouse models. Detailed work<sup>32</sup> with AAV2/5 and the gfaABC<sub>1</sub>D promoter to drive astrocyte specific gene expression suggested that two weeks post infection would be an ideal time to use in the present work (in future studies shorter and longer time points will also be evaluated). Thus following described methods<sup>32</sup>, we used adeno associated viruses of the 2/5 serotype (AAV2/5) that preferentially target astrocytes<sup>33,34</sup> together with the gfaABC<sub>1</sub>D promoter to deliver GFP–tagged Kir4.1 channels (Kir4.1–GFP) or cytosolic tdTomato as a control (Fig. 6a,b). After injection at P56, AAV2/5 mediated viral transduction lead to Kir4.1 and tdTomato expression in S100 $\beta$  positive astrocytes throughout the striatum (Supp Fig. 11; n = 4): we estimate that Kir4.1–GFP expressing astrocytes were present in  $83 \pm 1\%$  (n = 4) of the striatal volume. Kir4.1–GFP was not detected within striatal neurons (data not shown). Moreover, in astrocytes that were mHTT positive in R6/2 mice (white arrows 2 & 3 in Fig. 6b), AAV2/5 Kir4.1–GFP viruses increased Kir4.1 immunostaining to mean levels of  $15.2 \pm 0.9$  a.u. of fluorescence intensity (n = 35 cells from 4 mice), which was slightly, but not significantly, greater than the mean  $13.4 \pm 0.4$  a.u. (n = 147 cells from 6 mice) seen in WT mice (Fig. 5d) and was significantly greater than the mean  $11.1 \pm 0.7$  a.u. (n = 52 cells from 6 mice) detected in mHTT positive astrocytes from untreated R6/2 mice (Fig. 5d) ( $P = 0.0011$  with a two–tailed Mann–Whitney test). Thus, AAV2/5 Kir4.1–GFP viruses restored Kir4.1 immunostaining in astrocytes with mHTT nuclear aggregates to essentially normal levels.

The I/V relations of P60–80 R6/2 striatal astrocytes expressing Kir4.1–GFP were restored to levels equivalent to WT mice at P60–80 (Fig. 6c v Fig. 3c), whereas the I/V relations of astrocytes expressing tdTomato were the same as non-injected R6/2 mice at P60–80 (Fig. 6c). Moreover, expression of Kir4.1–GFP rescued deficits in astrocyte resting membrane potentials and macroscopic slope conductance of R6/2 mice (Fig. 6d,e v Fig. 3d). Finally, Ba<sup>2+</sup>–sensitive currents recorded from R6/2 astrocytes at P60–80 in Kir4.1–GFP expressing astrocytes were the same size as those recorded from WT mice, whereas in cells expressing tdTomato they were smaller and equal to those measured in un injected R6/2 mice (Fig. 6f,g,h v Fig. 4b).

We also carried out controls with the AAV Kir4.1–GFP and tdTomato viruses. Thus, AAV2/5 Kir4.1–GFP did not significantly increase total or Ba<sup>2+</sup> sensitive currents in WT astrocytes (Supp Fig 12a,b). Relative to mice that received AAV2/5 tdTomato, those that received Kir4.1–GFP displayed significant levels of GFP–tagged Kir4.1 and elevated levels of total Kir4.1 levels by Western blot analysis (Supp Fig 12c,d). Interestingly, astrocytes

expressing Kir4.1–GFP also displayed significantly elevated levels of Glut–1 levels as compared to those expressing tdTomato (Supp Fig 12e), implying that restoration of Kir4.1 function also rescues additional deficits in R6/2 mice. We evaluated whether AAV2/5 mediated delivery of Kir4.1–GFP caused inflammation in relation to WT and R6/2 mice, as well as in relation to R6/2 mice receiving AAV2/5 tdTomato, and found that it did not (Supp Fig 13).

### Elevated striatal K<sup>+</sup> levels in R6/2 mice and effects on MSNs

One of the proposed functions of astrocyte Kir4.1 channels is to maintain extracellular K<sup>+</sup> levels<sup>23</sup>. In light of this, we asked whether extracellular K<sup>+</sup> levels were elevated in the striatum of R6/2 mice at P60–80 relative to WT mice (Fig. 7a). Using K<sup>+</sup> selective microelectrodes<sup>22,35</sup> inserted into the striatum *in vivo*, we found that K<sup>+</sup> concentration was significantly elevated from  $1.5 \pm 0.2$  mM ( $n = 6$ ) in WT mice to  $2.9 \pm 0.3$  mM ( $n = 5$ ) in R6/2 mice at P60–80 (Fig. 7b;  $P = 0.0041$  unpaired Student's *t* test). This increase in R6/2 mice was ameliorated by injecting AAV2/5 Kir4.1–GFP (K<sup>+</sup> concentration was  $1.8 \pm 0.3$  mM;  $n = 5$ ,  $P > 0.05$  compared to WT, unpaired Student's *t* test). The doubling of the extracellular K<sup>+</sup> concentration would lead to a significant depolarization of  $E_K$ , hence, this discovery in R6/2 mice would be expected to alter neuronal excitability<sup>36</sup>.

Interestingly, one of the features of HD mouse models is that MSNs are 3 to 13 mV more depolarized than MSNs in WT mice<sup>14,37</sup>. We determined if a change in striatal K<sup>+</sup> concentration from 1.5 to 3.0 mM, as measured in R6/2 mice *in vivo* (Fig. 7b), could be sufficient to reproduce this effect in WT mice. If so, this would suggest that a hitherto overlooked underlying initial cause of depolarized MSNs may simply be a change in extracellular K<sup>+</sup> concentration (Fig. 7b). We made current–clamp recordings from MSNs in brain slices from WT mice and measured their resting membrane potentials in a bath solution containing 1.5 mM K<sup>+</sup>, then we switched to 3 mM K<sup>+</sup> and recorded a significant depolarization of  $\sim 6$  mV (Fig. 7e,f;  $n = 17$ ,  $P < 0.0001$  paired Student's *t* test). Changing the K<sup>+</sup> concentration also significantly changed the rheobase (Fig. 7c,d,g;  $n = 5$ ,  $P = 0.0032$ , paired Student's *t* test) – a change that mimics published differences observed for MSNs between HD mouse models and WT mice<sup>14,37</sup>. In summary, subtly elevating the extracellular K<sup>+</sup> concentration to the same levels that we measured in R6/2 mice *in vivo* (Fig. 7a,b) can phenocopy in WT mice several key MSN properties reported in HD mouse models.

### Attenuation of phenotypes in R6/2 mice by delivery of Kir4.1–GFP

A salient feature across mouse models of HD is that MSNs display depolarized membrane potentials by up to 12 mV<sup>8</sup>. We considered the possibility that reducing astrocyte Kir4.1 function with Ba<sup>2+</sup> in WT slices may reveal secondary consequences for MSNs, but this experiment is unfeasible (Supp Fig. 14). We therefore used a different approach to explore how dysfunction of astrocyte Kir4.1 channels in R6/2 mice affected MSNs. We measured deficits in MSN properties in HD mice in relation to WT, and then sought to determine if they can be rescued with AAV2/5 Kir4.1–GFP (Fig. 6). Recalling past work<sup>8</sup>, we found that MSNs from R6/2 mice were significantly depolarized by  $\sim 12$  mV, were more excitable and displayed higher membrane resistances compared to WT (Fig. 7h–j;  $n = 13–17$ ). Next, we

injected R6/2 mice with AAV2/5 Kir4.1–GFP or AAV2/5 tdTomato and then recorded from MSNs two weeks later (Fig. 7k–m;  $n = 19–20$ ). We found that MSN properties were significantly improved in mice that had been injected with AAV2/5 Kir4.1–GFP as compared to AAV2/5 tdTomato (Fig. 7k–m). Indeed, in the case of resting membrane potentials, expression of Kir4.1–GFP rescued MSNs to WT levels (Fig. 7h v Fig. 7k), but the rescue was partial in the case of excitability and membrane resistance (Fig. 7l,m). The differences in MSN properties observed by delivering Kir4.1–GFP channels to striatal astrocytes in R6/2 mice (Fig. 7) suggest that Kir4.1 channels may be promising targets to correct aspects of MSN dysfunction in HD, which in the simplest interpretation appear to involve astrocytes and neurons. It is likely that restoring astrocyte Kir4.1 function restores their homeostatic functions within the striatum, which has beneficial effects on MSNs. Additionally, neuron–astrocyte contacts can regulate ion channel expression within astrocytes<sup>21</sup>, raising the possibility that neuronal properties may be changed by contacting astrocytes with normal Kir4.1 levels<sup>38</sup>.

We next determined whether bilateral striatal injections of AAV2/5 Kir4.1–GFP to recover astrocyte Kir4.1 currents (Fig. 6) could lead to attenuation of HD phenotypes in male R6/2 mice. We assayed motor coordination using the rotarod<sup>39</sup> without practice sessions. Although practice can improve rotarod performance, untreated R6/2 mice sometimes seized and died immediately after falling off the rotarod and multiple training sessions would have exacerbated this. We used the paw clasp test (Supp Fig. 15) to measure dystonia/dyskinesia<sup>7</sup>. We used footprint analysis to evaluate gait. Using these assays, we compared WT with R6/2 mice, and also with R6/2 mice that had received either AAV2/5 Kir4.1–GFP or AAV2/5 tdTomato injected bilaterally into the striatum at P56. First, in all assays the R6/2 mice displayed severe deficits relative to WT mice, emphasizing HD phenotypes by P92 (Fig. 8, Supp Fig. 15). Second, we found that delivery of Kir4.1–GFP did not improve HD phenotypes in the rotarod or paw clasp assays (Supp Fig. 15). Third, using footprint analysis we found that Kir4.1–GFP expression improved both stride length and width in R6/2 mice to levels that were significantly better than both untreated R6/2 mice and R6/2 mice injected with AAV2/5 tdTomato (Fig. 8a–c). Fourth, from a specific set of experiments, when analyzed at ~51 days post injection, most of the R6/2 mice that had received AAV2/5 Kir4.1–GFP were alive, but most of the R6/2 mice that had received AAV2/5 tdTomato were dead, as expected for R6/2 mice of this age<sup>40</sup> ( $P < 0.0063$ , two-sided Fisher's Exact test; Fig. 8d). However, there were no differences in body weight between these groups for dead or living mice (Fig. 8e). For another different set of experiments, survival analysis also confirmed the increased longevity of R6/2 mice injected with AAV2/5 Kir4.1–GFP relative to those with AAV2/5 tdTomato (Fig. 8f;  $n = 11$  &  $10$ ), such that by 115 days after birth (~60 days post injection), ~80% of the R6/2 mice that had received AAV2/5 Kir4.1–GFP were alive, whereas, as expected<sup>40</sup>, only 22% of mice that received AAV2/5 tdTomato were alive ( $P < 0.0001$ , two-sided Fisher's Exact test). This was reflected by an increase in the average lifespan by ~8 days from  $98.7 \pm 5.7$  to  $116.5 \pm 4.5$  days for R6/2 mice that received tdTomato or Kir4.1–GFP, respectively (Fig. 8f;  $P = 0.0306$  with a one-tailed unpaired Mann-Whitney test). Thus, differences observed by delivering Kir4.1–GFP channels to striatal astrocytes in R6/2 mice (Fig. 8) suggest that motor



phenotypes in HD and HD-models are due to complex, multifactorial mechanisms that are likely to involve dysfunction of multiple cell types.

## Discussion

There are eight findings from this study. *First*, striatal astrocytes from R6/2 mice contain mHTT nuclear inclusions at P60–80, i.e. when the mice are symptomatic, but before detectable evidence of astrogliosis. *Second*, striatal astrocytes from symptomatic R6/2 mice display depolarized membrane potentials and lower membrane conductances. *Third*, striatal astrocyte electrophysiological defects can be accounted for by lower functional expression of Kir4.1 channels, and can be recovered by AAV2/5 mediated delivery of Kir4.1 to astrocytes. *Fourth*, extracellular K<sup>+</sup> buffering is reduced in the brains of R6/2 mice as evidenced by significantly elevated extracellular K<sup>+</sup> levels in the striatum at P60–80. *Fifth*, increasing K<sup>+</sup> concentrations in brain slices from healthy WT mice reproduced some of the features of altered MSN excitability observed in R6/2 mice. *Sixth*, all the key cellular observations with R6/2 model mice are reproduced in the Q175 mice when they are symptomatic, implying that these observations are not restricted to the aggressive R6/2 mouse model of HD. In future studies, many more aspects of astrocyte biochemistry and physiology need to be explored in both HD mouse models to determine if some phenotypic changes can be detected at presymptomatic stages in the less aggressive Q175 mode. If this were to be the case, then this would provide a basis to choose one mouse model over the other. *Seven*, expression of Kir4.1–GFP in astrocytes also rescued some MSN deficits observed in R6/2 mice. *Eight*, expression of Kir4.1–GFP within striatal astrocytes *in vivo* attenuated a HD-like motor deficit and prolonged survival in R6/2 mice. When interpreting these findings, it is important to remember that the functional measurements relied on whole-cell patch clamp electrophysiology that leads to intracellular dialysis of neurons and astrocytes. Therefore, the data need to be considered with this caveat in mind.

The study of HD is a rapidly developing field, but only limited attention has focused on astrocytes and their potential roles. Past studies have shown a disruption of astrocyte Glt–1 function<sup>11,41–43</sup> in HD mouse models, but the present study was motivated by the discovery that post mortem specimens from HD patients show mHTT inclusions in striatal astrocytes<sup>9,10</sup>. Moreover, expression of mHTT in astrocytes lead to death of co-cultured striatal neurons<sup>9</sup>, and expression of mHTT in astrocytes *in vivo* by employing the GFAP promoter lead to reduced Glt–1 expression<sup>10</sup>, age-dependent HD-like pathology and premature mortality<sup>11</sup>. By their nature these studies do not prove that astrocyte physiology is altered in, or if astrocytes contribute to, conventional mouse models of HD. Our aim was to confirm or refute the hypothesis that astrocyte physiology is altered in standard models of HD. Our second aim was to evaluate and provide hypotheses for exploring plausible causative roles of astrocytes in HD.

We found that GFAP did not label the majority of astrocytes in the mouse striatum. On the other hand, Aldh1L1, S100 $\beta$  and GS labeled most striatal astrocytes, recalling past experiences with Aldh1L1<sup>16</sup>. In R6/2 mice, mHTT nuclear inclusions were detected at P30 in ~10% of S100 $\beta$  positive astrocytes prior to the onset of symptoms and prior to detectable neurodegeneration. The astrocyte nuclear load of mHTT inclusions increased with time with

the onset and progression of symptoms and pathology in both R6/2 and Q175 mice. At a time point concomitant with the onset of symptoms (P60–80), significantly more astrocytes (~20%) displayed mHTT inclusions and exhibited significant reductions in important functional proteins such as GS, GLT-1, S100 $\beta$  and Kir4.1 than at a pre-symptomatic stage (P30). Single-cell analyses demonstrated a positive relation between the presence of mHTT nuclear inclusions in astrocytes and reductions in levels of Kir4.1 immunostaining. In contrast, GFAP levels were not significantly altered at this time (P60–80) and there were no other major phenotypic changes associated with astrocyte reactivity<sup>15</sup>. These findings suggest that mHTT is associated with early intrinsic disruption of the expression of important astrocyte functional proteins (e.g. Kir4.1, Glut-1), which alters astrocyte function without triggering astrogliosis. If so, later signs of astrogliosis in R6/2 mice at greater than P100 could derive from external cues resulting from increasingly severe local neurodegeneration. These data imply that pursuing therapeutic strategies aimed at early stages of the disease may be useful to correct functional deficits within astrocytes, with the possibility that subsequent astrogliosis may be reduced. Such approaches may be more fruitful than targeting the mechanisms of astrogliosis, which appears to be a heterogeneous<sup>44,45</sup>, context dependent and often protective response to a wide range of disparate insults<sup>15</sup>.

It is well established that in HD mouse models<sup>8</sup> MSNs are depolarized by up to ~12 mV, display lower membrane conductances and display lower K<sup>+</sup> currents<sup>46,47</sup>. In accord with the MSN data, using two HD mouse models before and during HD-like symptoms, we found that striatal astrocytes are depolarized by +5 mV and display lower membrane conductances by up to 20%. Our experiments show that the underlying cause of both these defects can be attributed to a loss of Kir4.1 functional expression within mHTT expressing striatal astrocytes. This result has clear implications for understanding HD and other neurological and psychiatric disorders, and speaks to the realization that astrocytes act in partnership with neurons in health and disease<sup>2,3</sup>. In future work, further mechanistic studies are needed to explore how Kir4.1 function and expression are robustly reduced in HD mouse models, even though mRNA levels did not decrease significantly in our evaluations. One possibility is that mHTT affects the trafficking or processing of Kir4.1 channels.

The loss of Kir4.1 currents in striatal astrocytes predicts reduced spatial K<sup>+</sup> buffering and higher ambient K<sup>+</sup> levels in HD mouse models<sup>23</sup>. We tested for this and found that the extracellular K<sup>+</sup> concentration was doubled in R6/2 mice. This prompted us to explore the impact of increased K<sup>+</sup> (from 1.5 to 3.0 mM) on the properties of MSNs in WT mice. To our surprise, we found that these changes reproduced the excitability features of MSNs described in a variety of HD mouse models<sup>8</sup>. Interestingly, brain wide astrocyte specific deletion of Kir4.1 channels causes mice to fall over, display hind leg splaying and “wobble”<sup>48</sup>, features that broadly phenocopy HD motor phenotypes in R6/2 mice<sup>7</sup>. To further explore the relationship between astrocyte Kir4.1 channels and HD-like phenotypes in R6/2 mice, we delivered Kir4.1-GFP channels to striatal astrocytes and found that one motor symptom (stride length and width) was attenuated by this approach. It seems unlikely that all motor phenotypes can be recovered by any one striatal-specific intervention, because R6/2 mice have multiple abnormalities. Moreover, we found that MSN membrane properties were also partly recovered by astrocytic expression of Kir4.1-GFP. These tantalizing

findings strongly support the notion that HD-like phenotypes derive from neuronal dysfunction that also involves astrocyte disturbances, pointing towards Kir4.1 as a promising target to potentially correct some deficits in HD.

To date, research efforts have been focused largely on identifying neuronal mechanisms to account for changes in MSN properties in HD models. Our findings provide compelling evidence for the novel hypothesis that key aspects of altered MSN excitability in HD are secondary to disturbance of astrocyte maintenance of extracellular  $K^+$ , which may have secondary consequences for MSNs such as through glutamate transport. These findings have important implications for therapeutic strategies in HD and suggest that therapeutics that target only disturbances of MSNs are likely to be inadequate or suboptimal as regards restoring function and ameliorating disease symptoms.

## Online Methods

### Mouse models

R6/2 and non-transgenic control mice were obtained from in house breeding (JAX, Bar Harbor, Maine). In some cases, R6/2 and WT mice were purchased from Jackson Laboratories directly at the appropriate ages. Mice were genotyped by PCR and CAG repeat length determined by Laragen (Culver City, CA). The CAG repeat length of mutant offspring was between 118 and 140. Q175 mice, homozygous, heterozygous and non-transgenic controls were also bred in house by crossing heterozygous males and females as obtained from JAX. Mice were genotyped by PCR and CAG repeat length determined by Laragen. The CAG repeat length of mutant offspring was between 170 and 208. Experiments conducted according to protocols approved by the Chancellor's Animal Research Committee of the Office for Protection of Research Subjects at UCLA.

### Histology and immunohistochemistry

For histological evaluations, mice were euthanized by barbiturate overdose and perfused transcardially with PBS, followed by 10% buffered formalin (Fisher). Brains were removed, post-fixed overnight and cryoprotected in buffered 30% sucrose for at least 2 days. 40  $\mu$ m coronal frozen sections were prepared using a cryostat microtome (Leica, Nussloch Germany) and either stained with cresyl violet or processed for brightfield or fluorescence immunohistochemistry. Briefly, brightfield immunohistochemistry was performed using biotinylated secondary antibodies (Vector, Burlingame, CA), biotin-avidin-peroxidase complex (Vector) and diaminobenzidine (DAB, Sigma) as the developing agent. Fluorescence immunohistochemistry was performed using secondary antibodies tagged with Alexa 488 (green), Alexa 350 (blue) (Molecular Probes, Grand Island NY), Cy3 (red), or Cy5 (far-red) (Vector Labs, Burlingame CA). The nuclear stain, 4',6'-diamidino-2-phenylindole dihydrochloride (DAPI; 2 ng/ml; Molecular Probes), was used to label nuclei. The following primary antibodies were used: rabbit anti-GFAP (1:1000, Dako, Carpinteria CA); mouse anti-GFAP (1:500, Sigma, CA); rabbit anti-Kir4.1 (1:400, Alomone Labs, Jerusalem, Israel); sheep anti-S100 $\beta$  (1:600, QED Bioscience; Atlanta, GA); mouse anti-S100 $\beta$  (1:400, Sigma); rabbit anti-GLT-1 (1:1000, Millipore); mouse anti-glutamine synthetase (1:400, Millipore; Billerica, MA); rabbit anti-glutamine synthetase (1:400,

Millipore); mouse anti-mHTT (clone EM48; 1:200, Millipore); mouse anti-mHTT (clone MW8; 1:50, DSHB, Iowa), rabbit anti-Iba1 (1:1,000, Wako), rat anti-CD68 (1:150, Serotec), rabbit anti-Aldh1L1 (1:200, Abcam, Cambridge MA); mouse anti-Ki67 (1:1000, Vector Labs; (Burlingame, CA); rabbit anti-pSTAT3 (1:1000, Millipore). Stained sections were examined and photographed using brightfield, fluorescence and laser scanning confocal microscopy (Zeiss, Oberkochen Germany).

### Quantitative morphometric evaluations

The number of astrocytes with mHTT nuclear inclusions was quantified by evaluating stacks of consecutive 1  $\mu\text{m}$  confocal microscopic images acquired with a 63X objective lens and taken from random fields of caudate putamen that had been triple stained for mHTT, S100 $\beta$  and DAPI. All S100 $\beta$  stained astrocytes within a 63X field were evaluated. Astrocytes with one or more mHTT positive inclusion bodies were scored as mHTT positive. At least 30 astrocytes were evaluated per animal and at least 4 animals were evaluated per group. The relative intensity of Kir4.1 immunofluorescence was quantified in astrocytes that were positive or negative for mHTT by evaluating 1  $\mu\text{m}$  confocal microscopic images acquired with a 63X objective lens and taken from random fields of caudate putamen that had been quadruple stained for Kir4.1, mHTT, S100 $\beta$  and DAPI. S100 $\beta$  positive astrocytes were identified and classified as mHTT positive or negative. The area of individual astrocyte was then traced on the basis of S100 $\beta$  staining followed by measuring the integrated density of the Kir4.1 immunofluorescence using Image J software v1.30 (NIH).

### Western blot analysis

For evaluation of protein expression by Western blot analysis, mice were euthanized by barbiturate overdose and brains rapidly removed and placed into ice cold PBS. Caudate putamen fresh tissue was rapidly dissected bilaterally in PBS on ice under 10X magnification (Zeiss, Oberkochen Germany) and tissue samples were rapidly frozen on dry ice. Total protein was extracted from individual tissue samples using a lysis buffer (50 mM Tris-HCL, 150 mM NaCl, 1% Nonidet P-40, 10 mM NaF, 10 mM EDTA, 0.5 mM dithiothreitol (DTT), 1 mM sodium orthovanadate Na<sub>3</sub>VO<sub>4</sub>, 1 mM phenylmethylsulfonyl fluoride (PMSF), 4  $\mu\text{g}/\text{ml}$  leupeptin and 4  $\mu\text{g}/\text{ml}$  pepstatin A, pH 7.4) and centrifuged at 12,000 g for 25 minutes at 4°C. The supernatant was used for measurements of protein. Protein concentration was determined using a Bio-Rad DC protein kit (Bio-Rad Laboratories, Hercules, CA). Protein preparations were separated by sodium dodecyl sulfate polyacrylamide gel electrophoresis (SDS-PAGE) and transferred to a polyvinylidene difluoride (PVDF) membrane and blocked with 5% nonfat milk TBST buffer and probed using various antibodies. The primary antibodies used for Western blotting were: rabbit anti-GFAP (1:1000, Dako); rabbit anti-Kir4.1 (1:1000, Alomone Labs); mouse anti-S100  $\beta$  (1:800, Sigma); rabbit anti-Glt1 (1:10,000, Millipore); mouse anti-glutamine synthetase (1:1000, Millipore); rabbit anti-actin (1:500; Sigma). Western blots were visualized using Amersham ECL Western Blotting Analysis System (Amersham Pharmacia Biotech) and exposed to Kodak X-ray film. Equivalence of protein loading was corrected for by probing for  $\beta$ -actin. For quantification, the optical density of the gel bands was determined using ImageJ Software v1.30 (NIH).

### Preparation of brain slices for electrophysiology

Striatal slices were prepared from P30 to P80 wild type and R6/2 mice. Briefly, animals were deeply anesthetized and decapitated. The brains were placed in ice-cold modified artificial cerebrospinal fluid (aCSF) containing (in mM): 194 sucrose, 30 NaCl, 4.5 KCl, 1 MgCl<sub>2</sub>, 26 NaHCO<sub>3</sub>, 1.2 NaH<sub>2</sub>PO<sub>4</sub> and 10 D-glucose, and cut into 300 μm thick coronal slices containing the striatum and cortex. For Q175 mice which were older than 6 months, the cutting buffer used protective artificial cerebrospinal fluid (aCSF) of the following composition (in mM): 92 N-methyl-D-glucamine (NMDG), 2.5 KCl, 1.25 NaH<sub>2</sub>PO<sub>4</sub>, 30 NaHCO<sub>3</sub>, 20 HEPES, 25 glucose, 2 thiourea, 5 Na-ascorbate, 3 Na pyruvate, 0.5 CaCl<sub>2</sub>, and 10 MgSO<sub>4</sub>·7H<sub>2</sub>O. The pH of the solution was titrated to 7.3–7.4 with concentrated HCl (which provides Cl<sup>-</sup> counter-ions for NMDG). Brain slices were allowed to equilibrate for at least 1 h at room temperature in normal aCSF containing (in mM): 124 NaCl, 4.5 KCl, 2 CaCl<sub>2</sub>, 1 MgCl<sub>2</sub>, 26 NaHCO<sub>3</sub>, 1.2 NaH<sub>2</sub>PO<sub>4</sub> and 10 D-glucose continuously bubbled with a mixture of 95% O<sub>2</sub>/5% CO<sub>2</sub> gas.

### Electrophysiological recording from astrocytes and MSNs in brain slices

For striatal astrocyte recordings from R6/2 and Q175 mice, currents were measured in whole-cell mode using pipettes with a typical resistance of 5–6 MΩ when filled with internal solution containing (in mM): 130 KCl, 2 MgCl<sub>2</sub>, 10 HEPES, 5 EGTA, 2 Na-ATP, 0.5 CaCl<sub>2</sub>, with pH set to 7.3. Cells were visualized with infrared optics on an upright microscope (BX51WI, Olympus). pCLAMP10 software and a MultiClamp 700B amplifier was used for electrophysiology (Axon Instruments). For striatal medium spiny neuron recordings, the ACSF contained the following (in mM): 125 NaCl, 2.5 KCl, 2 CaCl<sub>2</sub>, 1 MgCl<sub>2</sub>, 25 NaHCO<sub>3</sub>, 1.25 NaH<sub>2</sub>PO<sub>4</sub>, and 12.5 glucose. Pipettes were filled with a K<sup>+</sup> internal solution consisting of (in mM) 135 K-gluconate, 5 KCl, 0.5 CaCl<sub>2</sub>, 5 HEPES, 5 EGTA, 2 Mg-ATP, and 0.3 Na-GTP, pH 7.3 adjusted with KOH.

### In vivo K<sup>+</sup> concentration measurements

K<sup>+</sup>-sensitive electrodes were made according to a procedure described earlier<sup>22,49,50</sup>. In short, double-barreled glass capillaries (borosilicate theta glass, OD 1.5 mm, ID 1 mm, septum 0.2 mm, Warner Instruments Inc., Hamden CT) were washed for 6–24 hours in 1 M HCl and rinsed in 70% ethanol. Next they were dried for 6–8 hours at 100–120°C and stored for up to 4 weeks in desiccated containers. Pipettes were pulled (DMZ Universal Puller, Zeitz, Martinstried, Germany) from these capillaries and tips were broken under a stereomicroscope until each barrel had a 1–2 μm opening. After filling the tips for a length of ~1 cm with silanization solution I (5% dimethyldichlorosilane in heptane, Sigma-Aldrich), the microelectrodes were dried at 100–120°C for 6–10 hours. The final step of the K<sup>+</sup>-electrode production was done directly before use. The tip of one barrel was filled for a length of 2–10 μm with the K<sup>+</sup>-ionophore I-cocktail B (5% valinomycin, 93% 1,2-dimethyl-3-nitrobenzene, 2% potassium tetrakis(4-chlorophenyl)borate, Sigma Aldrich), and backfilled with 200 mM KCl; the other barrel (reference electrode) was filled with saline solution (150 mM NaCl). The potential over the two barrels was measured using AgCl-electrodes with a high impedance differential amplifier (model 3000, A-M Systems, Carlsborg, WA). Signals were filtered with a 0.1 Hz low-pass filter (on amplifier) and

sampled at 1 Hz (NI USB–6009 DAC–board and Labview software, National Instruments, Austin TX) and stored for later analysis. Analyses was made using Microsoft Excel (Microsoft, Albuquerque NM). The  $K^+$ –electrodes were calibrated by stepping the electrodes through a series of solutions with different  $K^+$ –concentrations (KCl in mM: 100, 30, 10, 3, 1, and 0.3; NaCl was added to each solution to bring the ionic strength to a total of 100 mM; pH 7.3, buffered with 10 mM HEPES). The relationship between concentration and voltage over both barrels was derived using the Nicolsky–Eisenman equation. Only electrodes with at least a 50 mV/p[ $K^+$ ] and linear response in the range from 1–3 p[ $K^+$ ] were used.

Surgeries were performed under aseptic conditions on the various mice (see Results) according to a protocol approved by the University of California, Los Angeles Chancellor's Animal Research Committee. Each animal was deeply anesthetized with isoflurane and affixed in a stereotaxic frame (Stoelting Co., Wood Dale, IL). Body temperature was maintained at 36–37°C (measured rectally) using a water circulating heating pad. For placement of the  $K^+$ –electrode we used coordinates as described earlier to record evoked field potentials from the striatum. To assure the correct location of the  $K^+$ –electrode, we stimulated the cortico–striatal pathway via a stimulus electrode (bipolar twisted pair tungsten, Plastics One, Roanoke, VA) placed in the prelimbic area of the medial prefrontal cortex (1.7–2.1 mm anterior to bregma, 0.4 lateral to midline, 2.0 mm ventral to the cortical surface, ipsilateral to the striatal recording hemisphere) to evoke field potentials in the striatum. While stimulating the cortico–striatal pathway (300  $\mu$ s pulse width, 400 mA pulse amplitude every 30 s, with a 365 stimulus isolator, WPI, Sarasota, FL) the  $K^+$  electrode was placed in the rostral area of the dorsal striatum at an angle of 20° in the coronal plane (0.6–1.1 mm anterior to bregma, 1.0–3.0 mm lateral to midline, 1.5–4.0 mm ventral to the cortical surface). Large evoked field potentials recorded with the reference channel of the  $K^+$ –electrode confirmed the correct striatal placement of the electrode. After correct placement, the stimulation was switched off, we waited 25–30 min for a stable baseline (which typically happened in 10 min) and then the local  $K^+$  concentration was measured. After the measurements, the  $K^+$ –electrode was removed and calibrated (see above). Results were only accepted if all calibration points before and after the *in vivo* measurements showed a deviation of less than 10%.

### HEK–293 cell culture, transfection and whole–cell voltage–clamp recordings

HEK–293 cells (ATCC) were maintained in 75 cm<sup>2</sup> cell culture flasks in Dulbecco's modified Eagle's medium/F12 media with Glutamax (Invitrogen) supplemented with 10% Fetal Bovine Serum and 1% penicillin/streptomycin. Cells were prepared for transfection by plating onto 6 well plates at the time of splitting, 3 to 4 days before transfection. They were transfected at ~60% confluence. For transient expression in HEK–293, we used ~0.3  $\mu$ g of plasmid and the Effectene transfection reagent (Qiagen). When appropriate, 100 ng of YFP was used as a marker of transfected cells. The manufacturer's instructions (Qiagen) were followed. Cells were gently dispersed and plated on poly–D–lysine coated glass coverslips (12 mm diameter). HEK–293 cell extracellular recording solution comprised (in mM) NaCl 147, KCl 2, MgCl<sub>2</sub> 1, CaCl<sub>2</sub> 1, Hepes 10, and glucose 10 (pH 7.4), and the pipette solution contained (in mM) KCl 154, EGTA 11, and Hepes 10. Whole–cell voltage–clamp

recordings were made with 3 to 5 M $\Omega$  borosilicate glass electrodes (World Precision Instruments), with an Axopatch 200B amplifier controlled by a computer running pCLAMP 8.1 software via a Digidata 1322A interface (Axon Instruments). Data were filtered at 2 kHz and digitized at > 5 kHz. The cells were used 3 days post transfection. Waiting longer than this was not possible because the cells became too sick to patch.

### AAV 2/5 generation and microinjections in vivo

Adeno-associated viruses of the 2/5 serotype, utilizing the minimal gfaABC<sub>1</sub>D promoter and capable of expressing tdTomato and Kir4.1-GFP specifically within astrocytes were generated and employed using described procedures<sup>32</sup>. R6/2 mice at P56 were used in all experiments in accordance with institutional guidelines. All surgical procedures were conducted under general anesthesia using continuous isoflurane (induction at 5%, maintenance at 1–2.5% vol/vol). Depth of anesthesia was monitored continuously and adjusted when necessary. Following induction of anesthesia, the mice were fitted into a stereotaxic frame with their heads secured by blunt ear bars and their noses placed into an anesthesia and ventilation system (David Kopf Instruments, Tujunga CA). Mice were administered 0.05 ml of buprenorphine (Buprenex®, 0.1 mg/ml) subcutaneously prior to surgery. The surgical incision site was then cleaned 3 times with 10% povidone iodine and 70% ethanol. Skin incisions were made, followed by craniotomies of 2–3 mm in diameter above the left parietal cortex using a small steel burr (Fine Science Tools) powered by a high-speed drill (K.1070, Freedom). Saline (0.9%) was applied onto the skull to reduce heating caused by drilling. Unilateral viral injections were carried out by using a stereotaxic apparatus (David Kopf Instruments) to guide the placement of beveled glass pipettes (1B100–4, World Precision Instruments) into the left striatum (the coordinates were (from the Bregma): anterior–posterior +0.8 mm, medial–lateral +2 mm, and dorsal–ventral –2.4 mm from the pial surface). 2  $\mu$ l of AAV2/5 gfaABC<sub>1</sub>D TdTomato or AAV2/5 gfaABC<sub>1</sub>D Kir4.1-GFP ( $\sim 10^{13}$  gc/ml) was injected by using a syringe pump (Pump11 PicoPlus Elite, Harvard Apparatus). Glass pipettes were left in place for at least 10 mins. Surgical wounds were closed with single external 5–0 nylon sutures. Following surgery, animals were allowed to recover overnight in cages placed partially on a low-voltage heating pad. Buprenorphine was administered 2 times per day for up to 2 days after surgery. In addition, Trimethoprim Sulfamethoxazole (40 and 200 mg, respectively per 500 ml water) was dispensed in the drinking water for one week. Mice were sacrificed 12–20 days post-surgery for electrophysiology or immunohistochemistry (typically 13–15 days). When assessing mouse behavior, AAVs were injected bilaterally, but otherwise the protocol was exactly the same.

### Real-time quantitative PCR (qPCR)

RNA was extracted from striatal tissue samples using Qiagen All Prep DNA/RNA Mini Kit. 200 ng of mRNA was converted into cDNA using Invitrogen Superscript VILO cDNA synthesis kit. cDNA was diluted 1:2 with DEPC treated water. Applied Biosystems Taqman probes were used with Taqman Universal Mastermix II, no UNG. qPCR was performed on Applied Biosystems 7900HT. Cycling parameters were: 50°C for 2 min, 95°C for 10 min, 40 repeats of 95°C for 15 seconds and 60°C for 1 minute. GADPH, ATP5B and UBC were

used as controls. Ct method was utilized to determine Relative Fold Expression of mRNA.

### Behavioral analysis

**Limb clasping analysis**—Mice were tested for limb clasping behavior by holding the mice from the tail and suspending them for 60 seconds. The time taken to clasp their forelimbs towards their belly was measured.

**Motor function analysis**—Mouse motor coordination was assessed by using the accelerating rotarod test and footprint test<sup>39</sup>. Briefly, in the accelerating rotarod test, each mouse was placed on a single lane rotarod (Med Associates) for three trials per session. The rotarod was set for constant acceleration from 3.0 to 30 rpm over a 5-min period and animals were scored in seconds to fall. Mice were not exposed to rotarod practice sessions. It is possible that practice may have improved performance in R6/2 mice with AAV-Kir4.1, but repeated sessions would likely also have killed a number of the sicker untreated mice. We found that some untreated R6/2 mice seized and died immediately after falling of the rotarod. Training sessions would have exacerbated this. For gait analysis, each mouse with nontoxic red paint on forepaws and black paint on the hind paws was required to run along a paper-lined runway (3 feet long and 3 inches wide) to obtain an edible treat in a dark goal box at the end. The footprints were analyzed to collect stride length and width and all statistical evaluations were performed with unpaired Student's *t* test. The CAG repeat length for the cohort of mice used at the time behavioral analyses were performed was  $125.9 \pm 0.3$  CAGs (mean  $\pm$  s.e.m;  $n = 82$  mice) with a range of 119–132 CAG repeats. The behavioral experiments were done blind during the day between the hours of 9 am and 9 pm.

### Data analysis

All statistical tests were run in GraphPad InStat 3. The graphs were created in Origin 8 and assembled in CorelDraw 12. Data are presented as mean  $\pm$  s.e.m. For each set of data to be compared we determined within GraphPad InStat whether the data were normally distributed or not. If they were normally distributed we used parametric tests, as listed in the text. If the data were not normally distributed we used non parametric tests, as indicated in the text. Paired and unpaired Student's two tailed *t* tests (as appropriate and as indicated in the text) and two tailed Mann–Whitney tests were used for most statistical analyses with significance declared at  $P < 0.05$ , but stated in each case in the figures and text. We decided which test to use based on whether the data were normally distributed or not. No statistical methods were used to pre-determine sample sizes but our sample sizes are similar to those reported in previous publications<sup>7,13</sup>. Data collection and analysis were not performed blind to the conditions of the experiments. However, behavioral analyses and experiments were performed blind to the experiment. Data were collected and processed randomly and were not assigned to blocks.

### Drugs and chemicals

All chemical were purchased from Sigma–Aldrich, Tocris–Cookson or VWR.



## Supplementary Material

Refer to Web version on PubMed Central for supplementary material.

## Acknowledgments

This work was supported mainly by the CHDI Foundation (BSK, MVS, XT, YA) and partly by the NIH (NS060677, MH104069 to BSK). Thanks to Dr. P Kofuji for sharing Kir4.1–GFP plasmids. Thanks to R Korsak for coordinating the genotyping. Thanks to Drs. V Beaumont, I Munoz–Sanjuan, MS Levine, C Cepeda, E Shigetomi and all current and past members of the Khakh and Sofroniew labs for discussions.

## References

1. Kuffler SW. Neuroglial cells: physiological properties and a potassium mediated effect of neuronal activity on the glial membrane potential. *Proc R Soc Lond B Biol Sci.* 1967; 168:1–21. [PubMed: 4382871]
2. Barres BA. The mystery and magic of glia: a perspective on their roles in health and disease. *Neuron.* 2008; 60:430–440. [PubMed: 18995817]
3. Ransom BR, Ransom CB. Astrocytes: multitasking stars of the central nervous system. *Methods Mol Biol.* 2012; 814:3–7. [PubMed: 22144296]
4. Maragakis NJ, Rothstein JD. Mechanisms of Disease: astrocytes in neurodegenerative disease. *Nat Clin Pract Neurol.* 2006; 2:679–689. [PubMed: 17117171]
5. Ilieva H, Polymenidou M, Cleveland DW. Non-cell autonomous toxicity in neurodegenerative disorders: ALS and beyond. *J Cell Biol.* 2009; 187:761–772. [PubMed: 19951898]
6. Clarke LE, Barres BA. Emerging roles of astrocytes in neural circuit development. *Nat Rev Neurosci.* 2013; 14:311–321. [PubMed: 23595014]
7. Mangiarini L, et al. Exon 1 of the HD gene with an expanded CAG repeat is sufficient to cause a progressive neurological phenotype in transgenic mice. *Cell.* 1996; 87:493–506. [PubMed: 8898202]
8. Cepeda C, Cummings DM, André VM, Holley SM, Levine MS. Genetic mouse models of Huntington's disease: focus on electrophysiological mechanisms. *ASN Neuro.* Apr 7.2010 2(2):e00033.10.1042/AN20090058 [PubMed: 20396376]
9. Shin JY, et al. Expression of mutant huntingtin in glial cells contributes to neuronal excitotoxicity. *J Cell Biol.* 2005; 171:1001–1012. [PubMed: 16365166]
10. Faideau M, et al. In vivo expression of polyglutamine-expanded huntingtin by mouse striatal astrocytes impairs glutamate transport: a correlation with Huntington's disease subjects. *Hum Mol Genet.* 2010; 19:3053–3067. [PubMed: 20494921]
11. Bradford J, et al. Expression of mutant huntingtin in mouse brain astrocytes causes age-dependent neurological symptoms. *Proc Natl Acad Sci U S A.* 2009; 106:22480–22485. [PubMed: 20018729]
12. Pouladi MA, Morton AJ, Hayden MR. Choosing an animal model for the study of Huntington's disease. *Nat Rev Neurosci.* 2013; 14:708–721. [PubMed: 24052178]
13. Menalled LB, et al. Comprehensive Behavioral and Molecular Characterization of a New Knock-In Mouse Model of Huntington's Disease: zQ175. *PLoS ONE.* 2012; 7(12):e49838.10.1371/journal.pone.0049838 [PubMed: 23284626]
14. Heikkinen T, et al. Characterization of Neurophysiological and Behavioral Changes, MRI Brain Volumetry and 1H MRS in zQ175 Knock-In Mouse Model of Huntington's Disease. *PLoS ONE.* 2012; 7(12):e50717.10.1371/journal.pone.0050717 [PubMed: 23284644]
15. Sofroniew MV. Molecular dissection of reactive astrogliosis and glial scar formation. *Trends Neurosci.* 2009; 32:638–647. [PubMed: 19782411]
16. Cahoy JD, et al. A transcriptome database for astrocytes, neurons, and oligodendrocytes: a new resource for understanding brain development and function. *J Neurosci.* 2008; 28:264–278. [PubMed: 18171944]

17. Wang CE, et al. Suppression of neuropil aggregates and neurological symptoms by an intracellular antibody implicates the cytoplasmic toxicity of mutant huntingtin. *J Cell Biol.* 2008; 181:803–816. [PubMed: 18504298]
18. Shigetomi E, Tong X, Kwan KY, Corey DP, Khakh BS. TRPA1 channels regulate astrocyte resting calcium and inhibitory synapse efficacy through GAT-3. *Nature Neuroscience.* 2011; 15:70–80. PMID pending. [PubMed: 22158513]
19. Higashi K, et al. An inwardly rectifying K(+) channel, Kir4.1, expressed in astrocytes surrounds synapses and blood vessels in brain. *Am J Physiol Cell Physiol.* 2001; 281:C922–931. [PubMed: 11502569]
20. Poopalasundaram S, et al. Glial heterogeneity in expression of the inwardly rectifying K(+) channel, Kir4.1, in adult rat CNS. *Glia.* 2000; 30:362–372. [PubMed: 10797616]
21. Barres BA, Koroshetz WJ, Chun LL, Corey DP. Ion channel expression by white matter glia: the type-1 astrocyte. *Neuron.* 1990; 5:527–544. [PubMed: 1698397]
22. Chever O, Djukic B, McCarthy KD, Amzica F. Implication of Kir4.1 channel in excess potassium clearance: an in vivo study on anesthetized glial-conditional Kir4.1 knock-out mice. *J Neurosci.* 2010; 30:15769–15777. [PubMed: 21106816]
23. Kofuji P, Newman EA. Potassium buffering in the central nervous system. *Neuroscience.* 2004; 129:1045–1056. [PubMed: 15561419]
24. Furutani K, Ohno Y, Inanobe A, Hibino H, Kurachi Y. Mutational and in silico analyses for antidepressant block of astroglial inward-rectifier Kir4.1 channel. *Mol Pharmacol.* 2009; 75:1287–1295. [PubMed: 19264848]
25. Su S, et al. Inhibition of astroglial inwardly rectifying Kir4.1 channels by a tricyclic antidepressant, nortriptyline. *J Pharmacol Exp Ther.* 2007; 320:573–580. [PubMed: 17071817]
26. Estrada-Sánchez AM, Rebec GV. Corticostriatal dysfunction and glutamate transporter 1 (GLT1) in Huntington's disease: interactions between neurons and astrocytes. *Basal Ganglia.* 2012; 2:57–66. [PubMed: 22905336]
27. Benn CL, Fox H, Bates GP. Optimisation of region-specific reference gene selection and relative gene expression analysis methods for pre-clinical trials of Huntington's disease. *Mol Neurodegener.* 2008; 3:17.10.1186/1750-1326-3-17 [PubMed: 18954449]
28. Strand AD, et al. Expression profiling of Huntington's disease models suggests that brain-derived neurotrophic factor depletion plays a major role in striatal degeneration. *J Neurosci.* 2007; 27:11758–11768. [PubMed: 17959817]
29. Tang TS, et al. Huntingtin and huntingtin-associated protein 1 influence neuronal calcium signaling mediated by inositol-(1,4,5) triphosphate receptor type 1. *Neuron.* 2003; 39:227–239. [PubMed: 12873381]
30. Rubinsztein DC, Carmichael J. Huntington's disease: molecular basis of neurodegeneration. *Expert Rev Mol Med.* 2003; 5:1–21. [PubMed: 14585171]
31. Adermark L, Lovinger DM. Electrophysiological properties and gap junction coupling of striatal astrocytes. *Neurochem Int.* 2008; 52:1365–1372. [PubMed: 18396351]
32. Shigetomi E, et al. Imaging calcium microdomains within entire astrocyte territories and endfeet with GCaMPs expressed using adeno-associated viruses. *J Gen Physiol.* 2013; 141:633–647. [PubMed: 23589582]
33. Ortinski PI, et al. Selective induction of astrocytic gliosis generates deficits in neuronal inhibition. *Nat Neurosci.* 2010; 13:584–591. [PubMed: 20418874]
34. Xie Y, Wang T, Sun GY, Ding S. Specific disruption of astrocytic Ca<sup>2+</sup> signaling pathway in vivo by adeno-associated viral transduction. *Neuroscience.* 2010; 170:992–1003. [PubMed: 20736051]
35. Hall DG. Ion-selective membrane electrodes: A general limiting treatment of interference effects. *Journal of Physical Chemistry.* 1996; 100:7230–7236.
36. Hille, B. *Ion channels of excitable membranes.* 3rd. Sinauer Associates, Inc.; 2001.
37. Klapstein GJ, et al. Electrophysiological and morphological changes in striatal spiny neurons in R6/2 Huntington's disease transgenic mice. *J Neurophysiol.* 2001; 86:2667–2677. [PubMed: 11731527]
38. Barres BA. Five electrophysiological properties of glial cells. *Ann N Y Acad Sci.* 1991; 633:248–254. [PubMed: 1724128]

39. Herrmann JE, et al. STAT3 is a critical regulator of astrogliosis and scar formation after spinal cord injury. *J Neurosci*. 2008; 28:7231–7243. [PubMed: 18614693]
40. Stack EC, et al. Chronology of behavioral symptoms and neuropathological sequela in R6/2 Huntington's disease transgenic mice. *J Comp Neurol*. 2005; 490:354–370. [PubMed: 16127709]
41. Behrens PF, Franz P, Woodman B, Lindenberg KS, Landwehrmeyer GB. Impaired glutamate transport and glutamate-glutamine cycling: downstream effects of the Huntington mutation. *Brain*. 2002; 125:1908–1922. [PubMed: 12135980]
42. Miller BR, et al. Up-regulation of GLT1 expression increases glutamate uptake and attenuates the Huntington's disease phenotype in the R6/2 mouse. *Neuroscience*. 2008; 153:329–337. [PubMed: 18353560]
43. Bradford J, et al. Mutant huntingtin in glial cells exacerbates neurological symptoms of Huntington disease mice. *J Biol Chem*. 2010; 285:10653–10661. [PubMed: 20145253]
44. Hamby ME, et al. Inflammatory mediators alter the astrocyte transcriptome and calcium signaling elicited by multiple G-protein-coupled receptors. *J Neurosci*. 2012; 32:14489–14510. [PubMed: 23077035]
45. Zamanian JL, et al. Genomic analysis of reactive astrogliosis. *J Neurosci*. 2012; 32:6391–6410. [PubMed: 22553043]
46. Ariano MA, et al. Striatal potassium channel dysfunction in Huntington's disease transgenic mice. *J Neurophysiol*. 2005; 93:2565–2574. [PubMed: 15625098]
47. Ariano MA, Wagle N, Grissell AE. Neuronal vulnerability in mouse models of Huntington's disease: membrane channel protein changes. *J Neurosci Res*. 2005; 80:634–645. [PubMed: 15880743]
48. Djukic B, Casper KB, Philpot BD, Chin LS, McCarthy KD. Conditional knock-out of Kir4.1 leads to glial membrane depolarization, inhibition of potassium and glutamate uptake, and enhanced short-term synaptic potentiation. *J Neurosci*. 2007; 27:11354–11365. [PubMed: 17942730]
49. Amzica F, Steriade M. Neuronal and glial membrane potentials during sleep and paroxysmal oscillations in the neocortex. *J Neurosci*. 2000; 20:6648–6665. [PubMed: 10964970]
50. Amzica F, Steriade M. The functional significance of K-complexes. *Sleep medicine reviews*. 2002; 6:139–149. [PubMed: 12531149]

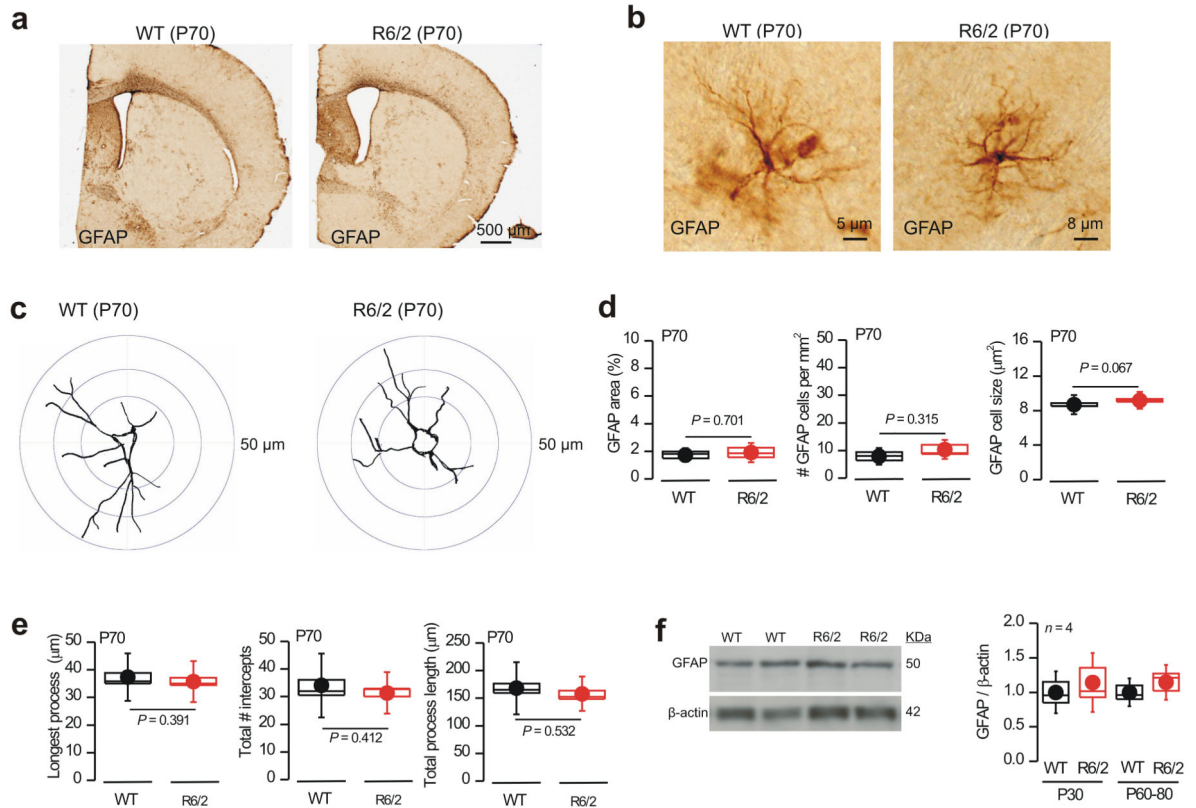


**Figure 1. No evidence for astrogliosis at symptomatic ages in R6/2 mice**

**a.** Brain sections from WT and R6/2 mice at P70 stained for GFAP using the DAB reaction.

**b.** Representative high magnification views of astrocytes from WT and R6/2 mice at P70.

R6/2 astrocytes exhibit no evidence of hypertrophy. **c.** Examples of Sholl analysis for

astrocytes stained for GFAP from images such as those in **b.** **d.** Quantification of GFAP

area, cells per mm<sup>2</sup> and soma size for images such as those in **b.** **e.** Quantification of key

parameters from Sholl analysis for images such as those in **c.** **f.** Western blot analysis of

GFAP expression in WT and R6/2 mice. The gels show data for P60 (in duplicate), whereas

the bar graph summarizes data at P30 and P60–80 (quantification was achieved by

normalizing to  $\beta$ -actin). The data shown in this figure were normally distributed and thus

statistical significance was assessed by unpaired Student's *t* test; *P* values are shown. For the

box and whisker plots shown here and elsewhere, the box is S.E.M and the whisker is S.D.

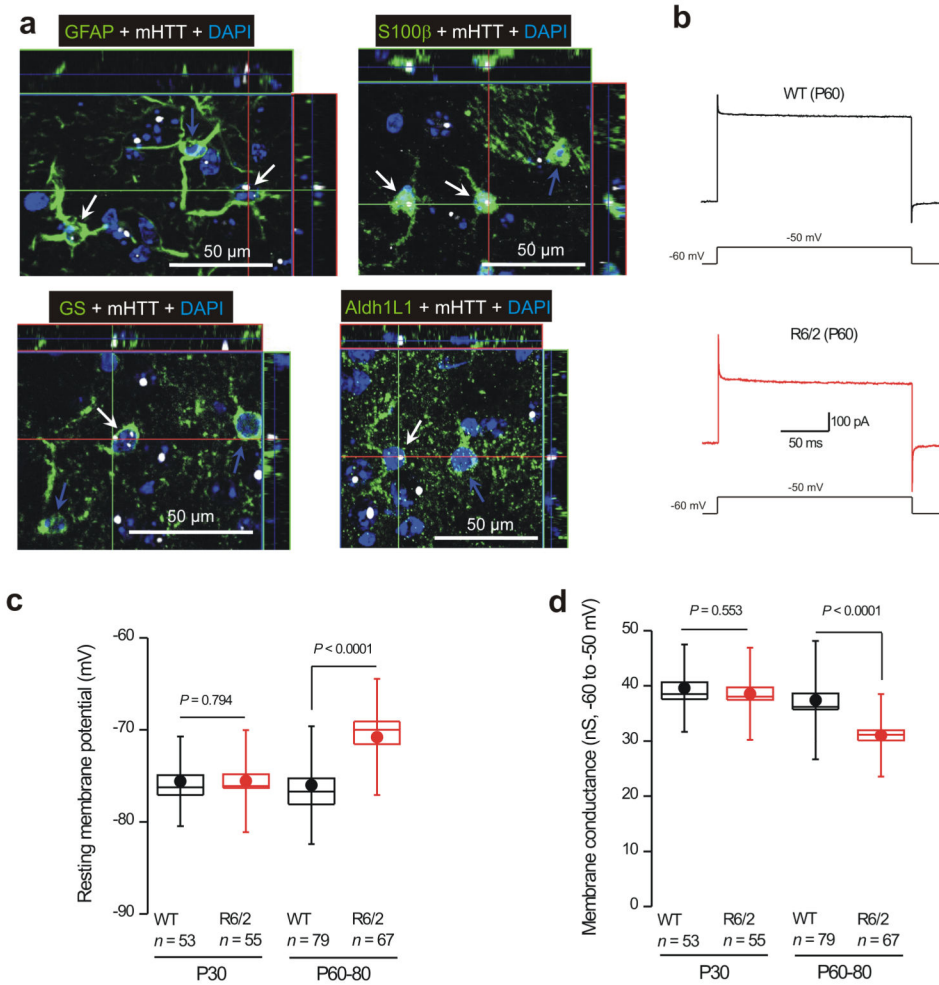


**Figure 2. Striatal astrocytes from R6/2 mice display nuclear mHTT inclusions, depolarized membrane potentials and lower membrane conductances**

**a.** Representative immunofluorescence images showing that GFAP, S100β, GS and Aldh1L1 labeled astrocytes (green) from R6/2 mice at P60 contain nuclear mHTT inclusions (nuclei were labeled blue with DAPI and mHTT is shown in white). **b** Representative traces of whole-cell voltage-clamp recordings from striatal astrocytes from WT and R6/2 mice at P60. The current waveforms show the response to a step depolarization, revealing clear differences between WT and R6/2 astrocytes. **c.** Graphs show striatal astrocyte resting membrane potentials for WT and R6/2 mice at the indicated ages. **d.** Membrane conductance between -60 and -50 mV for WT and R6/2 mice at the indicated ages. In **c** and **d**, the data are presented as mean ± S.E.M. The data in **c** and **d** were not normally distributed and statistical significance was assessed using the non parametric Two-tailed Mann-Whitney test; *P* values are indicated. For the box and whisker plots shown here and elsewhere, the box is the S.E.M and the whisker is the S.D.

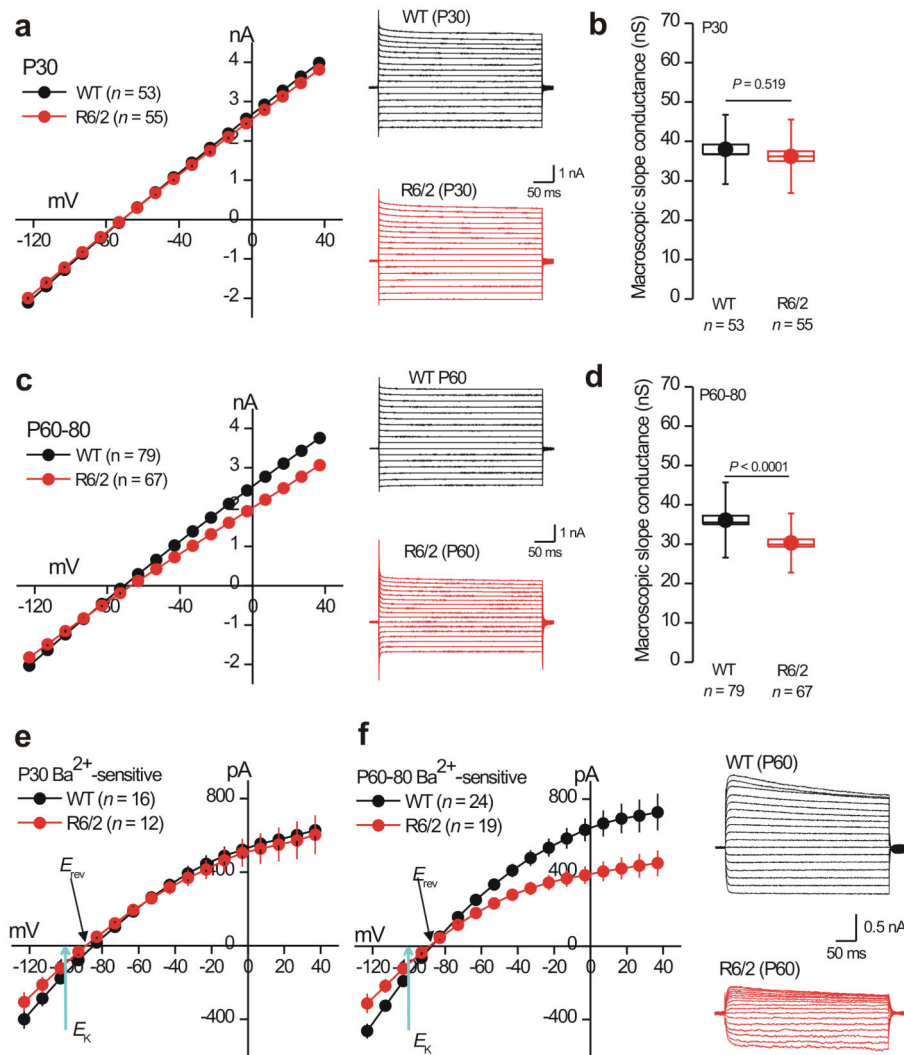


**Figure 3. Striatal astrocytes from R6/2 mice display reduced Ba<sup>2+</sup>-sensitive Kir4.1 currents at symptomatic ages (P60–80)**

**a.** I/V plots for WT and R6/2 striatal astrocytes at P30, with representative traces shown to the right. **b.** Histograms for membrane slope conductance calculated from the I/V plots for WT and R6/2 mice at P30 (between  $-120$  and  $+40$  mV). **c.** The graph shows I/V plots for WT and R6/2 striatal astrocytes at P60, with representative traces shown to the right. **d.** Histograms for membrane slope conductance calculated from I/V plots for WT and R6/2 mice at P60 (between  $-120$  and  $+40$  mV). **e.** I/V plots for Ba<sup>2+</sup>-sensitive currents for WT and R6/2 striatal astrocytes at P30. **f.** I/V plots for Ba<sup>2+</sup>-sensitive currents for WT and R6/2 striatal astrocytes at P60, with representative traces to the right. For the I/V plots, in some cases the error bars are smaller than the symbols used. In the case of b, d and f the data were not normally distributed and statistical significance was assessed using the non parametric Two-tailed Mann-Whitney test; *P* values are indicated. For the box and whisker plots shown here and elsewhere, the box is the S.E.M and the whisker is the S.D.

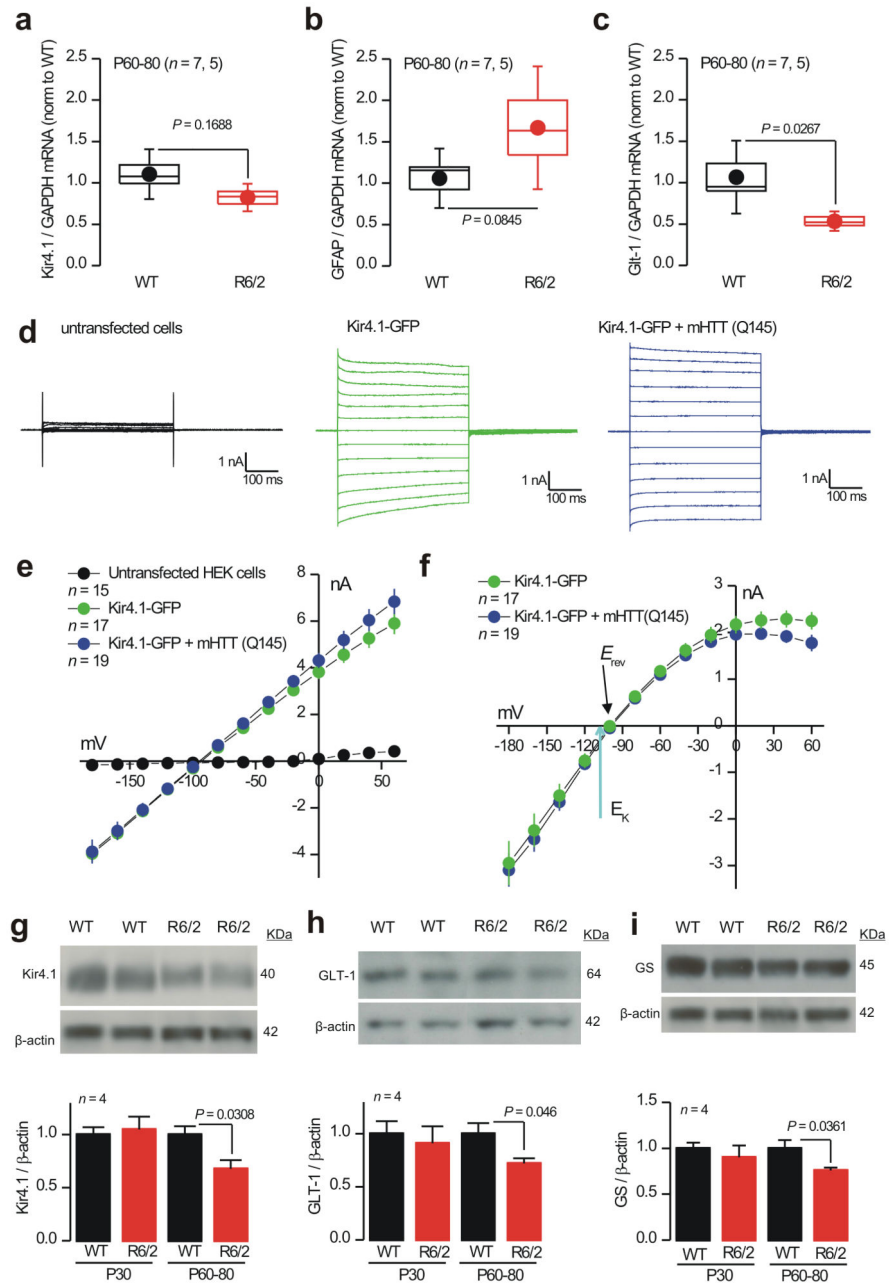


**Figure 4. Mechanistic studies of Kir4.1 currents in R6/2 mice and HEK-293 cells**  
**a–c.** qPCR data for Kir4.1 (**a**; gene name *KCNJ10*), GFAP (**b**) and Glt-1 (**c**) normalized to GAPDH levels for WT and R6/2 striatal tissue at P60–80. Additional RT–PCR experiments are shown in Supp Fig 8. **d.** Representative traces from HEK–293 cells that were untransfected, transfected with Kir4.1–GFP alone or cotransfected with Kir4.1–GFP plus mHTT(Q145). The current waveforms were elicited by step depolarizations from –160 to +60 mV (in 20 mV steps). **e.** Average I/V plots for experiments like those illustrated in **d**. **f.** Average  $Ba^{2+}$ -sensitive currents for HEK–293 cells expressing Kir4.1–GFP alone and Kir4.1–GFP plus mHTT(Q145). **g.** Representative Western blots and average data for Kir4.1

in WT and R6/2 mice at P30 and P60–80. **h.** As in **g**, but for GLT-1. **i.** As in **g**, but for GS. In the case of **g** and **h**, the data were not normally distributed and statistical significance was assessed using the non parametric Mann–Whitney test; *P* values are indicated. For the box and whisker plots shown here and elsewhere, the box is the S.E.M and the whisker is the S.D.



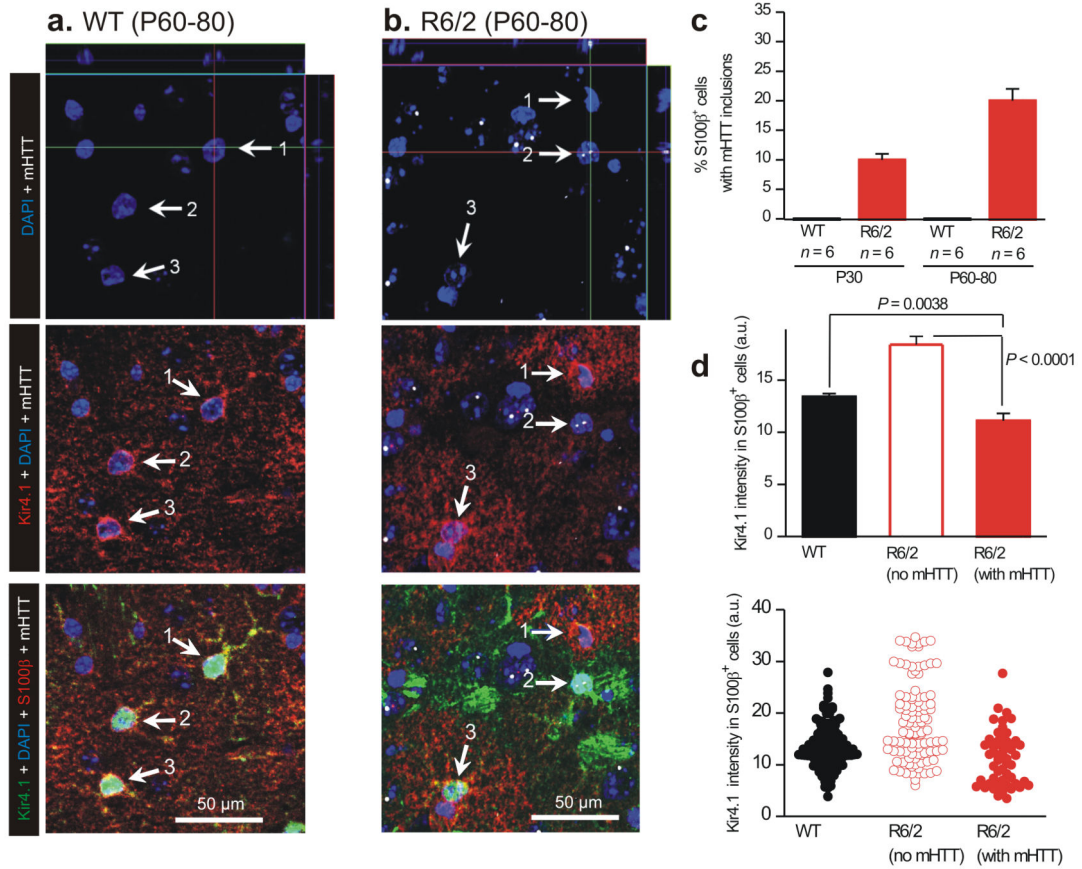


**Figure 5. Kir4.1 immunostaining is reduced in individual striatal astrocytes that contain nuclear mHTT inclusions**

**a.** Representative quadruple color immunofluorescence images of WT striatum at P60–80, labeled in the indicated colors for DAPI, Kir4.1, S100β and mHTT, showing that no cells expressed mHTT. White arrows (1–3) point to S100β positive cells that were also Kir4.1 positive (red). **b.** As in **a**, but for R6/2 striatum at P60–80 and showing that many cells were mHTT-positive. Some mHTT positive cells were S100β-positive and had much reduced Kir4.1 immunostaining (e.g. white arrow 2), whereas other S100β-positive cells lacked mHTT and displayed normal Kir4.1 immunostaining (white arrows 1,3). Are the images shown truly representative? When considering this, please note that the absolute intensity in the red channel (for Kir4.1) corresponding to cells 1, 2 and 3 was 28.2, 12.4 and 24.3 arbitrary units. Thus, these representative examples are within the distribution of all the data shown in panel d. Note also that none of the images shown in this figure (or elsewhere) have been adjusted or altered to exaggerate the fluorescence signal of any component channel. **c.** Plots the percentage of S100β positive cells that also contained mHTT nuclear inclusions in WT and R6/2 mice at P30 and P60–80. **d.** Plots Kir4.1 immunostaining intensity for WT mice at P60–80, as well as for S100β positive astrocytes that contained or did not contain mHTT. In the case of d the data were not normally distributed and statistical significance was assessed using the non parametric Two-tailed Mann-Whitney test; *P* values are indicated.

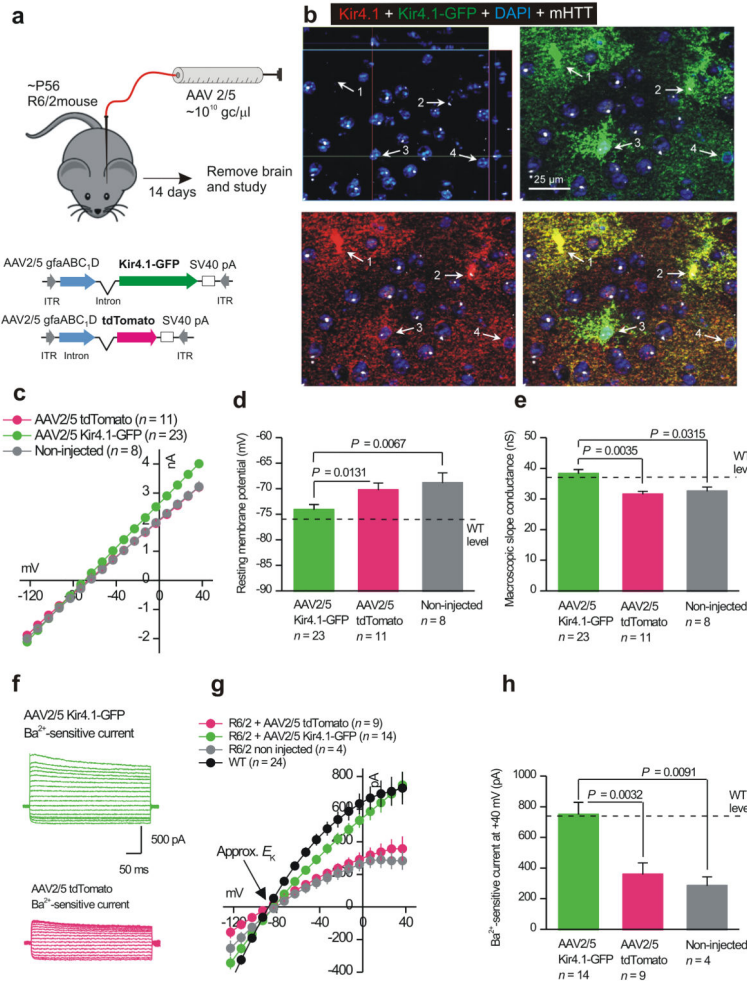


**Figure 6. AAV2/5 mediated Kir4.1-GFP expression rescues deficits observed in striatal astrocytes from R6/2 mice at P60-80**

**a.** The cartoon illustrates the viral constructs employed and the general protocol for AAV delivery into the striatum of adult R6/2 mice, which were microinjected at P56 and studied 14 days later. **b.** Immunostaining for total Kir4.1 (i.e. native Kir4.1 and that delivered with AAVs) following AAV2/5 Kir4.1-GFP microinjections in R6/2 striatum. Kir4.1 levels are restored to those of WT (see Fig. 5a) in mHTT positive astrocytes. **c-e.** The graphs show that AAV2/5 mediated delivery of Kir4.1-GFP to astrocytes significantly restored IV relations (**c**), membrane potentials (**d**) and membrane slope conductances (**e**) to control levels from WT mice. **f-h.** Representative traces (**f**), average I/V plots (**g**) and analysis of Ba<sup>2+</sup>-sensitive currents (**h**) shows that AAV2/5 mediated delivery of Kir4.1-GFP restored Ba<sup>2+</sup>-sensitive currents to levels almost identical to WT striatal astrocytes at P60-80. In panel **g**, the WT data are re plotted from Fig. 3f for comparison purposes. In the case of **d**, **e** and **h** the data were normally distributed and statistical significance was assessed using the unpaired Student's *t* test; *P* values are indicated.

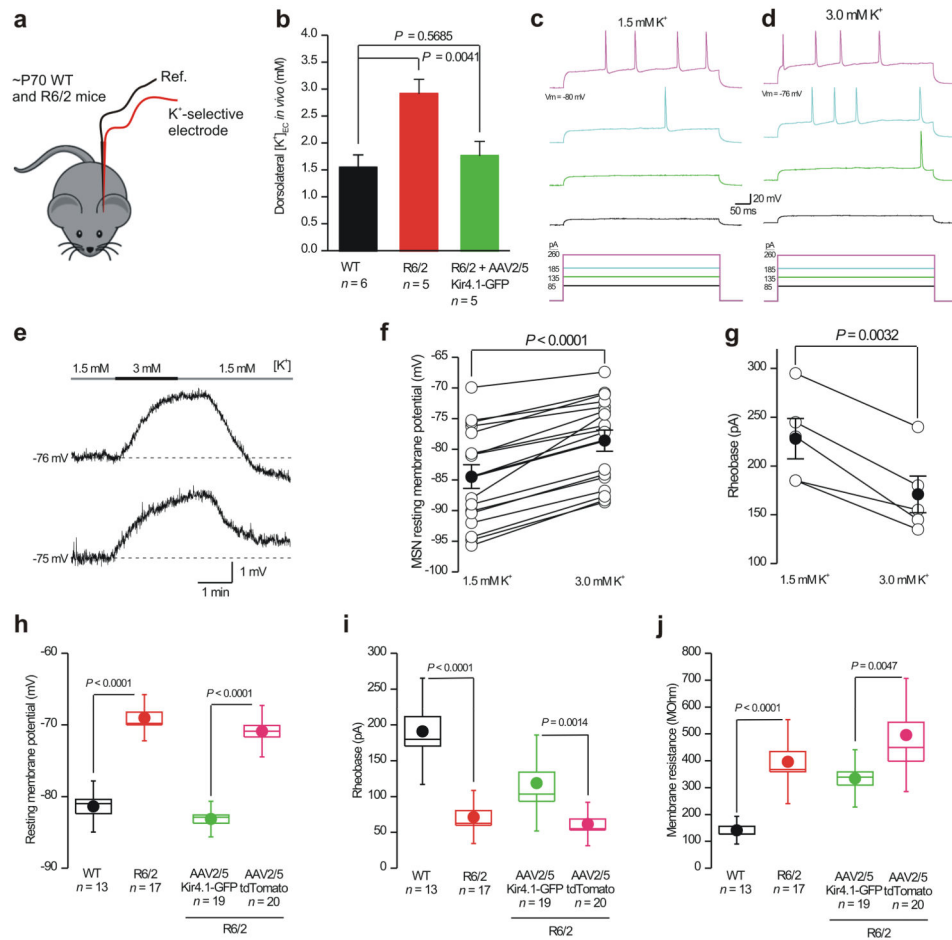


**Figure 7. Elevated striatal extracellular  $K^+$  levels in R6/2 mice *in vivo* and their effects on WT MSN excitability *in vitro***

**a.** The cartoon illustrates that we measured  $K^+$  concentrations *in vivo* in the striatum of WT and R6/2 at P60–80 using  $K^+$  selective microelectrodes. **b.** The graph shows  $K^+$  concentration measurements from WT, R6/2 and in R6/2 mice that had received Kir4.1–GFP. **c–g.** Representative traces (**c,d,e**) and average data (**f**) showing that subtly increasing the extracellular  $K^+$  concentration from 1.5 to 3.0 mM significantly depolarized MSNs, leading to a decrease in the depolarizing current needed to evoke action potentials (**c,d**) and significantly lowering the rheobase (**g**). **h–j.** Histograms show differences in the basic properties of MSNs from WT and R6/2 mice and the basic MSN properties from R6/2 mice that were injected with AAV2/5 Kir4.1–GFP versus those that received AAV2/5 tdTomato. In the case of f–j, the data were normally distributed and statistical significance was assessed using the paired (**f,g**) and un paired (**h–j**) Student's *t* tests; *P* values are indicated. For the box and whisker plots shown here and elsewhere, the box is S.E.M and the whisker is S.D.

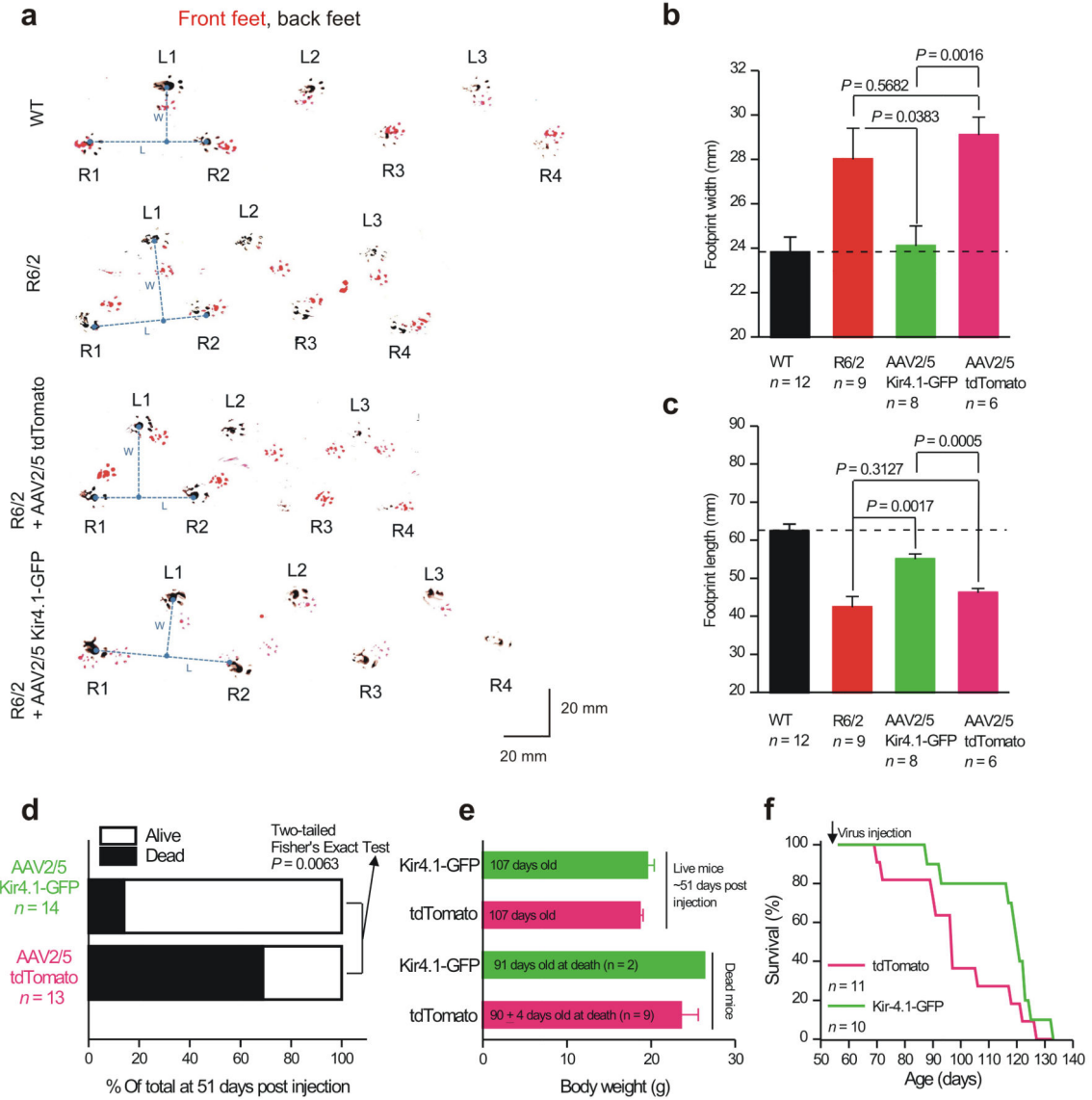


**Figure 8. AAV2/5 mediated Kir4.1-GFP expression attenuates a motor phenotype in R6/2 mice at P92**

**a.** Representative raw data for footprint tracks of mice walking on paper with their front and rear paws painted with red and black paint, respectively. **b–c.** Average data from experiments such as those shown in (a) for footprint length and width. AAV2/5 Kir4.1-GFP significantly improved stride length and width in relation to R6/2 mice and in relation to mice that received control AAV2/5 tdTomato virus microinjections. In the case of b and c the data were normally distributed and statistical significance was assessed using unpaired Student's t tests; *P* values are indicated. **d.** Statistical analysis of mouse survival for the indicated conditions: more mice survived from the pool that received AAV2/5 Kir4.1-GFP. **e.** Analysis of body weights (for dead and living mice) for the indicated conditions: there were no differences. **f.** Survival curves for R6/2 mice that received AAV2/5 tdTomato and AAV2/5 Kir4.1-GFP.